CHEMISTRY OF MATERIALS
Cite This: Chem. Mater. 2019, 31, 7962−7969
Article
pubs.acs.org/cm

Surface Science and Colloidal Stability of Double-Perovskite $Cs_2AgBiBr_6$ Nanocrystals and Their Superlattices

Yangning Zhang,[†] Tushti Shah,[†] Francis Leonard Deepak,[‡] and Brian A. Korgel*[,†]

[†]McKetta Department of Chemical Engineering and Texas Materials Institute, The University of Texas at Austin, Austin, Texas 78712-1062, United States

[‡]Nanostructured Materials Group, Department of Advanced Electron Microscopy, Imaging and Spectroscopy, International Iberian Nanotechnology Laboratory, Braga 4715-330, Portugal

Supporting Information

ABSTRACT: Capping ligand bonding and the thermal and colloidal stability of $Cs_2AgBiBr_6$ nanocrystals were studied. Oleylamine and oleic acid bonding to $Cs_2AgBiBr_6$ nanocrystals was studied with ^1H nuclear magnetic resonance and nuclear Overhauser effect spectroscopy. Both molecules are present in the ionic metathesis synthesis reaction, but only oleylamine remains bound to the nanocrystals after purification. Oleic acid is not a capping ligand; however, the synthesis requires it, and its concentration determines the yield of the reaction while oleylamine primarily affects the uniformity of the sample. Substitution of oleic acid in the reaction with diisooctylphosphinic acid still yielded nanocrystals with similar size, cuboidal shape, uniformity, cubic double-perovskite crystal structure, and optical properties. Nanocrystals were assembled into superlattices and heated in air. Grazing incidence small-angle and wide-angle X-ray scattering showed that the nanocrystals sinter at 250 °C, but the crystal structure and preferred crystal orientation on the substrate does not change. When nanocrystals were dispersed in hexane and exposed to light, they precipitated within 24 h. Scanning electron microscopy showed that the aggregated nanocrystals still retained their initial size and shape and had not coalesced.

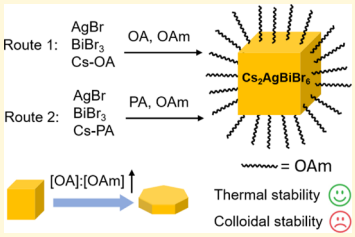

INTRODUCTION

Lead halide perovskites have remarkable optoelectronic properties[1−6] suitable for solar cells,[7,8] light-emitting diodes,[9] lasers,[10] and photodetectors.[11] A significant amount of research has been devoted to the study of nanocrystals of these materials as well, given their additional size-dependent properties and phase stability.[4,6,8,12,13] Yet, the toxicity of Pb and the poor stability of these materials in the presence of humidity remain a concern.[14,15]

Pb^{2+} can be substituted with tin or germanium, but the resulting compounds are even more unstable and susceptible to oxidation.[16,17] Compounds with much greater stability have been made by replacing two Pb^{2+} cations with one monovalent and one trivalent species. These double perovskites have the chemical formula $A_2B^{1+}B^{3+}X_6$.[18] At least 14 stable compounds like this have been predicted, including those with Cu^+, Ag^+, Au^+, or Tl^+ in B^{1+} sites and In^{3+}, Sb^{3+}, or Bi^{3+} in B^{3+} sites.[19] Among these alternatives, $Cs_2AgBiBr_6$ has been one of the easiest to make and study.

Bulk crystals of $Cs_2AgBiBr_6$ were first produced in 2016.[20,21] It has an indirect band gap of 1.95 eV, long photoluminescence (PL) lifetimes of ∼600 ns, and good stability to heat and moisture. $Cs_2AgBiBr_6$ has also been incorporated into solar cells, although the efficiencies have been modest (power conversion efficiencies of ∼2.5%).[22,23] Last year, colloidal $Cs_2AgBiBr_6$ nanocrystals were made.[24−26] Two other Ag-containing double-perovskite nanocrystals have also been reported, $Cs_2AgInCl_6$[27,28] and $Cs_2AgSbCl_6$.[28] Mn^{2+} doping was shown to enhance the PL of $Cs_2AgInCl_6$.[27] Here, we examine in some detail the roles of oleylamine (OAm) and oleic acid (OA) commonly used in the synthesis of $Cs_2AgBiBr_6$, and the thermal and colloidal stability of the nanocrystals.

EXPERIMENTAL DETAILS

Materials. Cesium carbonate (Cs_2CO_3, Sigma, 99.9% trace metal basis), silver bromide (AgBr, Alfa Aesar, 99.9985 metal basis), bismuth(III) bromide ($BiBr_3$, Sigma, 98%), 1-octadecene (ODE, $C_{18}H_{36}$, Sigma, 90%), OAm ($C_{18}H_{35}NH_2$, Sigma, 70%), OA ($C_{18}H_{34}O_2$, Sigma, 90%), diisooctylphosphinic acid (PA, $C_{16}H_{35}O_2P$, Sigma, 90%), hexane (C_6H_{14}, Sigma, 95%, anhydrous), chloroform-*d* [$CDCl_3$, Sigma, 99.8 at. % D, contains 0.03% (v/v) tetramethylsilane (TMS)], and methyl acetate ($C_3H_6O_2$, Sigma, 99.5%, anhydrous) were purchased and used as received. Transmission electron microscopy (TEM) grids were continuous carbon-coated 200 mesh copper grids (Electron Microscopy Science, LOT# 180307). Silicon wafer substrates (University Wafer) were p-type with 650 μm thickness and ⟨100⟩ orientation.

Preparation of Cs−Oleate and Cs-PA Complexes. Stock solutions of Cs−oleate (Cs−OA) and Cs−PA complexes were prepared by adding 0.814 g (2.5 mmol) of Cs_2CO_3, 40 mL of ODE, and 2.5 mL of OA or 2.5 mL of PA to a three-neck 100 mL flask. The mixture is heated to 120 °C for 1 h under vacuum and then to 150 °C under nitrogen. After the mixture turned from cloudy to clear, which

Received: June 3, 2019
Revised: September 12, 2019
Published: September 13, 2019

DOI: 10.1021/acs.chemmater.9b02149
Chem. Mater. 2019, 31, 7962−7969

means that Cs_2CO_3 has complexed with OA (or PA), the mixture is removed from the heating mantle and allowed to cool to room temperature for storage in a nitrogen-filled glovebox until needed.

Synthesis of $Cs_2AgBiBr_6$ Nanocrystals. $Cs_2AgBiBr_6$ nanocrystals were synthesized using procedures developed by Bekenstein, et al.[25] ODE (5 mL), AgBr (0.02 g, 0.11 mmol), and $BiBr_3$ (0.09 g, 0.20 mmol) were added to a 25 mL three-neck flask, heated to 110 °C under vacuum for 15 min, and then blanketed with nitrogen. In a standard batch using an [OA]/[OAm] molar ratio of 2:1, 1.0 mL of OA (3.0 mmol) and 0.5 mL of OAm (1.5 mmol) were heated to 70 °C separately before being added to the reaction flask. The [OA]/[OAm] ratio was also varied in some reactions. We used 0.5 mL of OA and 0.5 mL of OAm for 1:1 ratio, 1.0 mL of OA and 0.25 mL of OAm for 4:1 ratio, and 1.0 mL of OA and 0.125 mL of OAm for 8:1 ratio. The reaction mixture was placed again under vacuum at 110 °C for 5 min and then blanketed with nitrogen. The temperature was raised to 200 °C, and 0.5 mL (0.06 mmol) of the Cs−oleate stock solution (preheated to 100 °C) was added. After 3 min, when the reaction mixture turns yellow, the flask is removed from the heating mantle and immersed in a water bath at room temperature. For the reactions in which OA was substituted with PA, 1.0 mL (3.1 mmol) of PA was injected (instead of OA) with OAm at 110 °C, and 0.5 mL (0.06 mmol) of Cs−PA was injected instead of Cs−oleate at 200 °C.

The nanocrystals were separated from the crude reaction mixture by centrifugation at 4000 rpm (2057*g* for rcf, *g* being gravity) for 5 min. The nanocrystals settle out as a precipitate. The supernatant is discarded and the precipitate redispersed in 3 mL of hexane. Methyl acetate (1.5 mL) was added and the dispersion was again centrifuged at 8000 rpm (8228*g* for rcf) for 5 min. This time, the precipitate containing a black byproduct [see Supporting Information Figure S1 for X-ray diffraction (XRD)] was discarded. The supernatant is optically clear and has a golden color. More methyl acetate (1.5 mL) was added to the supernatant and centrifuged at 8000 rpm for 5 min. This serves as a size selection step, leading to the precipitation of the larger nanocrystals in the sample. After decanting the supernatant, the precipitated nanocrystals were redispersed in hexane and centrifuged again at 8000 rpm, this time to remove poorly capped nanocrystals. The supernatant was collected and stored sealed under nitrogen in a freezer. Reactions with OA typically yielded 7 mg of nanocrystals. The reactions with PA yielded about 6 mg of nanocrystals. Approximately 20−40 wt % of the nanocrystal product is residual solvent and organic ligand, as estimated based on thermogravimetric analysis (TGA) (see Supporting Information Figure S2). The molar conversion of reactants to $Cs_2AgBiBr_6$ is about 12−16%.

Nuclear Magnetic Resonance Spectroscopy and Nuclear Overhauser Effect Spectroscopy. ^{1}H NMR and nuclear Overhauser effect (NOESY) measurements were carried out using an Agilent VNMRS 600 spectrometer operated at 600 MHz. Nanocrystals were dispersed in chloroform-*d* at a concentration of 10 mg/mL. Nuclear magnetic resonance (NMR) data were acquired using a 90° pulse width, 2 s relaxation delay, and 64 scans. In NOESY, 1024 data points were collected in the direct dimension and 512 data points in the indirect dimension, with a spectral width of 9 ppm and a mixing time of 800 ms. NMR and NOESY spectra were processed using MestReNova software for subtraction of the background signal and calibration with the TMS peak.

Electron Microscopy. TEM was performed using an FEI Tecnai Biotwin TEM operated at 80 kV accelerating voltage for low-resolution images. JEOL 2010F TEM operated at 200 kV was used for high-resolution TEM, energy-dispersive X-ray spectroscopy (EDXS), scanning transmission electron microscopy (STEM) imaging, and elemental mapping. Scanning electron microscopy (SEM) images were acquired using the in-lens detector on a Zeiss Supra 40 VP SEM operated at 3 kV accelerating voltage. High-angle annular dark-field scanning transmission electron microscopy (HAADF−STEM) images were obtained on an FEI Titan G2 ChemiSTEM operated at 80 kV with a Cs probe corrector.

TEM samples were prepared by drop-casting dilute dispersions of nanocrystals in hexane onto the TEM grid. For SEM, samples were prepared by drop-casting concentrated dispersions of nanocrystals in hexane onto a silicon wafer. STEM imaging was carried out using TEM grids with nanocrystals deposited by drop-casting dilute dispersions in hexane followed by dipping in methyl acetate for several seconds to remove organic contamination.

X-ray Scattering. Powder XRD data were acquired using a Rigaku R-axis Spider diffractometer from $Cs_2AgBiBr_6$ nanocrystals drop-cast on a glass substrate. The X-ray generator was operated at 40 kV and 40 mA yielding Cu Kα radiation (λ = 1.54 Å). Samples were scanned for 10 min while rotating at 5° s^{-1}. 2DP and JADE software were used for background subtraction and data processing, respectively. Grazing incidence small-angle and wide-angle X-ray scattering (GISAXS and GIWAXS) was performed in vacuum using a SAXSLAB Ganesha SAXS−WAXS system. Monochromatic X-ray radiation of wavelength of 1.54 Å was used. The incident angle of the beam was 0.2°. Small- and wide-angle scattered photons were collected with a PILATUS3 R 300K detector with 487 × 619 pixels and a pixel size of 172 μm × 172 μm positioned at the appropriate distances from the sample (134 mm for GIWAXS and 1084 mm for GISAXS). FIT2D software (version: 12_077_i686_WXP) was used to process the patterns.[29,30]

Optical Measurements. UV−visible absorbance spectra were measured using a Varian Cary Bio (UV−vis) spectrophotometer. PL emission spectra were acquired using a Varian Cary Eclipse Fluorescence spectrometer. Nanocrystals were dispersed in hexane, toluene, or chloroform in a quartz cuvette with 1 cm path length for all optical measurements.

RESULTS AND DISCUSSION

Synthesis of $Cs_2AgBiBr_6$ Nanocrystals and Characterization of Their Shape and Crystal Structure. $Cs_2AgBiBr_6$ nanocrystals were synthesized by hot injection of cesium oleate into a mixture of AgBr and $BiBr_3$ in ODE, OA, and OAm at 200 °C[25]

$$3AgBr + 3BiBr_3 + 4Cs(RCOO) \xrightarrow[OA,OAm,ODE]{200°C,3min} 2Cs_2AgBiBr_6 + Ag(RCOO) + Bi(RCOO)_3$$
$$R = CH_3(CH_2)_7HC{=}CH(CH_2)_7 \quad (1)$$

This ionic metathesis reaction produces $Cs_2AgBiBr_6$ nanocrystals and silver oleate and bismuth oleate as byproducts. The nanocrystals were isolated and purified by precipitation with methyl acetate as an antisolvent instead of acetone or acetonitrile, which have also been used in the literature.[24,25] We have found that methyl acetate is less likely to lead to ligand desorption from perovskite nanocrystals and has been used to purify other perovskite nanocrystals, such as $CsPbBr_3$[31] and $CsPbI_3$[8] without degradation. Figure 1a shows a TEM image of $Cs_2AgBiBr_6$ nanocrystals obtained from this reaction and purification procedure. The nanocrystals are nearly perfect cubes with an average aspect ratio of 1.1 ± 0.1. The average lengths of the short and long edges of the cube-shaped nanocrystals are 9.0 ± 0.8 and 9.9 ± 1.0 nm. Figure 1b shows XRD of the nanocrystals, which is consistent with the cubic phase of $Cs_2AgBiBr_6$ ($Fm\bar{3}m$, a = 11.25 Å).[21] Peak fitting and size and strain analysis of the XRD pattern (see Supporting Information Figure S4 and Table S1) gives an estimated particle size of 10.4 nm, which is slightly larger than what we observed from TEM, and negligible microstrain.

Figure 2a,b show higher-resolution HAADF−STEM images of a field of $Cs_2AgBiBr_6$ nanocrystals. The nanocrystals are separated by capping ligands. The cube-shaped nanocrystals are terminated by six {100} facets. The nanocrystal in Figure 2c is viewed down the [001] direction bounded by its (200), (−200), (020), and (0−20) facets orthogonal to the substrate. The other two facets—(002) and (00−2)—are on the top and

DOI: 10.1021/acs.chemmater.9b02149
Chem. Mater. 2019, 31, 7962−7969

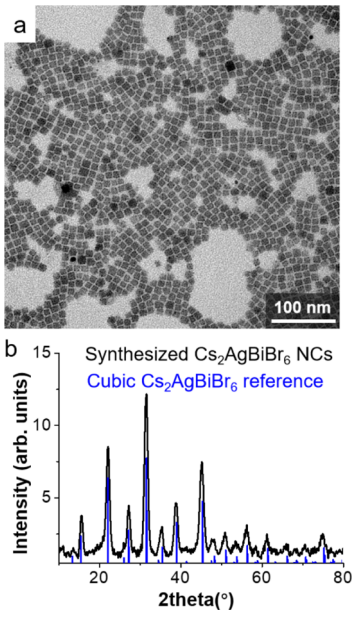

Figure 1. (a) TEM image of $Cs_2AgBiBr_6$ nanocrystals synthesized with OA and OAm. The nanocrystals have cubic shape with an average edge length of 9.7 ± 1.5 nm. (b) XRD of $Cs_2AgBiBr_6$ nanocrystals synthesized with OA and OAm. The reference pattern for cubic $Cs_2AgBiBr_6$ in blue is taken from Slavney, et al.[21]

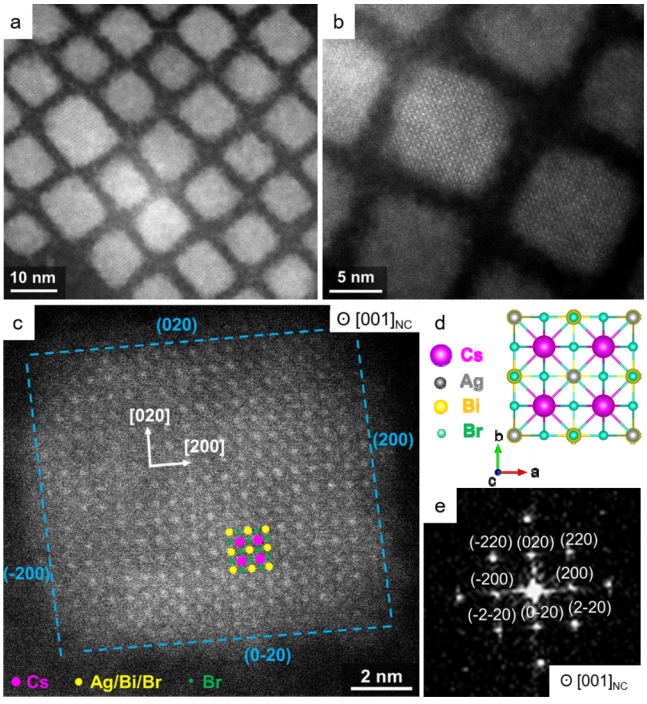

Figure 2. (a–c) HAADF–STEM images of $Cs_2AgBiBr_6$ nanocrystals synthesized with OA and OAm following the ionic metathesis reaction scheme of eq 1. (d) Illustration of the $Cs_2AgBiBr_6$ unit cell viewed down in the [001] direction. (e) FFT of (c) indexed to cubic $Cs_2AgBiBr_6$ with [001] zone axis. Atomic columns of Cs (magenta), mixed Ag/Bi/Br (yellow) and Br (green) atoms are observed in labeled in (c). The bonding crystal planes (light blue) of the nanocrystal correspond to (200), (−200), (020), and (0−20) facets.

bottom of the nanocrystal oriented parallel to the substrate. The columns of Cs atoms, mixed Ag/Bi/Br atoms, and Br atoms are visible in this crystal orientation, as shown in the crystal model provided in Figure 2d. The fast Fourier transform (FFT) of Figure 2c in Figure 2e indexes to cubic $Cs_2AgBiBr_6$ with [001] zone axis beam orientation. The high-resolution TEM image and FFT of an individual nanocrystal can be found in the Supporting Information, Figure S3. Electron beam induced degradation is often observed in these nanocrystals (Supporting Information, Figure S11).

OA and OAm Bonding to the Surface of $Cs_2AgBiBr_6$ Nanocrystals. For other perovskites, such as $CsPbBr_3$, some believe that both OA and OAm cap the nanocrystal surface,[33] while others argue that only OAm binds to nanocrystal surface.[34] In the case of $Cs_2AgBiBr_6$ nanocrystals, both OA and OAm are used in the synthesis, but we find that only OAm serves as a capping ligand for the $Cs_2AgBiBr_6$ nanocrystals. Figure 3a shows the ^{1}H NMR spectra of $Cs_2AgBiBr_6$ nanocrystals dispersed in chloroform-*d*. OAm and OA share similar signature peaks at 5.35 and 2.0 ppm corresponding to H atoms (**8**, **9**, **10**, and **11**) near the double bond (see the Supporting Information Figure S5 for ^{1}H NMR spectra of pure OAm and OA).[35] These protons are located relatively far from the nanocrystal surface and exhibit relatively sharp peaks in the as-purified sample.[35,36] The ^{1}H NMR signals from the amine group and the CH_2 closest to the amine group (labeled as α and β, respectively) at 6.8 and 3.7 ppm provide a unique signature of OAm. These peaks are perceptible but with significant peak broadening, indicating that OAm is bonded to the nanocrystal surface. The proton (**2**) closest to the carboxyl group provides a unique signal for OA. This peak is absent in the spectra of the purified nanocrystals. To determine if added OA would bond to the nanocrystals, 5 μL of OA was introduced into a dispersion of purified nanocrystals. A sharp triplet is observed at 2.35 ppm corresponding to (**2**). The lack of peak broadening of the triplet indicates that the added OA does not bond to the nanocrystal surface. Figure 3b shows this spectral region with higher magnification. Sharp peaks from residual ODE and hexane are also present in the spectra.

NOESY provides further evidence that OA does not bond to the $Cs_2AgBiBr_6$ nanocrystals. In NOESY, ligands bound to the NC surface have positive NOEs because of the positive cross-relaxation rate, while free ligand molecules have slightly negative or no NOEs because of a small negative or zero cross-relaxation rate.[32] Figure 3c shows the NOESY spectra for purified $Cs_2AgBiBr_6$ nanocrystals dispersed in chloroform-*d*. The positive (blue) cross peaks between OAm resonances confirm that OAm associates with the nanocrystal surface. There is no indication of OA associated with the nanocrystals. The NOESY spectra of pure OAm and OA only show the negative (red) cross peaks (see the Supporting Information, Figure S6).

Most likely, OAm binds to bromide on the nanocrystal surface as oleylammonium bromide to form an X-type ligand pair.[33] The association between OA and cationic species on the surface must also be very weak, as illustrated in Figure 3d. This mechanism of OAm ligand passivation on $Cs_2AgBiBr_6$ nanocrystals is most likely similar to that of $CsPbBr_3$ nanocrystals.[33,37] The main difference in capping ligand chemistry appears to arise from the difference in B-site cation composition.

Roles of OA and OAm in Determining the Reaction Yield, Nanocrystal Size, and Shape. The equilibrium between OA and OAm has been found to play an important role in determining the size, shape, and phase of $CsPbBr_3$ nanocrystals.[37] For $Cs_2AgBiBr_6$ nanocrystals, varying OA-to-

DOI: 10.1021/acs.chemmater.9b02149
Chem. Mater. 2019, 31, 7962−7969

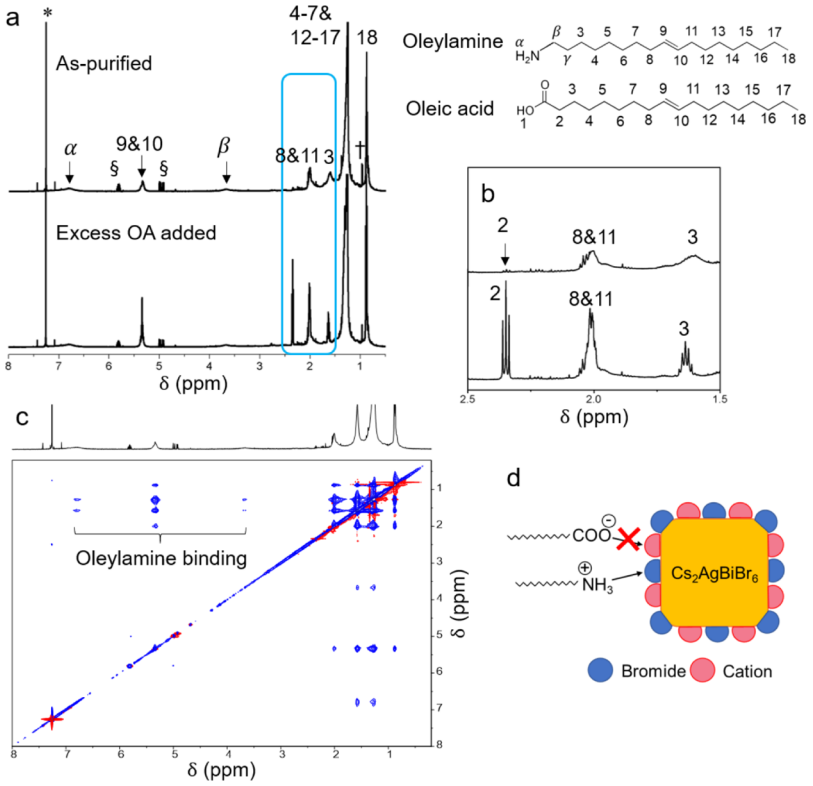

Figure 3. (a) ^{1}H NMR of as-purified $Cs_2AgBiBr_6$ nanocrystals and the same sample after adding 5 μL OA. The protons from OAm and OA are labeled with numbers. The broadened peaks of α and β protons of OAm indicate that OAm is bound to the nanocrystals. * is from chloroform-*d*. § is from residual ODE solvent. † is from the isomers of residual hexane solvent. (b) Enlarged view of 1.5−2.5 ppm region in (a). Before OA addition, the 2-proton of OA shows a tiny triplet peak, suggesting that OA is of very low concentration in the purified sample and not bound to the nanocrystals. After adding 5 μL of OA, the peak intensity increased significantly. (c) NOESY of as-purified $Cs_2AgBiBr_6$ nanocrystals. The blue cross peaks between the resonances of OAm showed that OAm is interacting with the surface of nanocrystals. (d) Schematic shows that OAm is bonded to the bromide of the nanocrystals, and OA is not bound to nanocrystals.

OAm ratio has been attempted with the trimethylsilyl-bromide injection method, and it has been found that a large excess of OA or OAm can both result in a significant amount of Cs−Bi−Br impurity.[24] We carried out reactions using a range of OA and OAm concentrations to determine the role of each species in the synthesis. Figure 4 shows the TEM images and histograms of the size distributions of the nanocrystals. The reaction yield was found to depend on the amount of OA, while the uniformity of the nanocrystals largely depended on the OAm concentration. In the standard reaction with a [OA]/[OAm] mole ratio of 2, the conversion is 14% and the nanocrystals are relatively uniform. Increasing [OA]/[OAm] from 2 to 4 to 8 led to larger average diameters of 9.7 to 15.3 to 17.0 nm, respectively, with more polydispersity and hexagonal or heptagonal shape. The [OA]/[OAm] ratio of four had the highest conversion of 26%. The XRD data were similar for all of these nanocrystals, matching cubic $Cs_2AgBiBr_6$. The absorbance spectra for all of the samples were also similar, with an absorption peak at 432 nm, corresponding to the Bi 6s−6p transitions in the $BiBr_6^{3-}$ complex.[25] The PL spectra of the three samples with [OA]/[OAm] ratios of 1, 2, and 4 showed a peak centered at 620 nm, but the peak intensity is slightly lower for the sample with an [OA]/[OAm] ratio of 4. We believe that this difference comes from the low OAm amount used in the synthesis and resulting defects in the nanocrystals that lead to surface traps and increased nonradiative electron−hole recombination. The sample with an [OA]/[OAm] ratio of 8 has a blue-shifted PL peak compared with the other three samples. This peak is likely coming from the ligand, while the nanocrystals are not emitting. EDXS and elemental mapping of the nanocrystals were carried out as well, which further confirmed that all the samples are composed of four elements Cs, Ag, Bi, and Br (see the Supporting Information, Table S2 and Figure S7). Reducing the mole ratio of [OA]/[OAm] from 2 to 1 produced more uniform nanocrystals with similar size, but much lower conversion of only 0.5%. On the basis of these data, the concentration of OAm largely determined the size and shape of the nanocrystals, while OA influenced the yield of the reaction.

Substituting OA with PA. To date, all literature reports of $Cs_2AgBiBr_6$ nanocrystal synthesis have used OA and OAm. We tried substituting other amines for OAm, such as dioctylamine and trioctylamine, but the products consisted of Cs−Bi−Br ternary compounds or a mixture of Cs−Bi−Br and $Cs_2AgBiBr_6$ that could not be separated. On the other hand, OA could be substituted with PA without any observable difference in the reaction product. PA has also been used in place of OA to make $CsPbI_3$ nanocrystals.[38] PA serves the same function as OA in the ionic metathesis reaction, by complexing with Cs as a starting material and stabilizing the reaction byproducts

DOI: 10.1021/acs.chemmater.9b02149
Chem. Mater. 2019, 31, 7962−7969

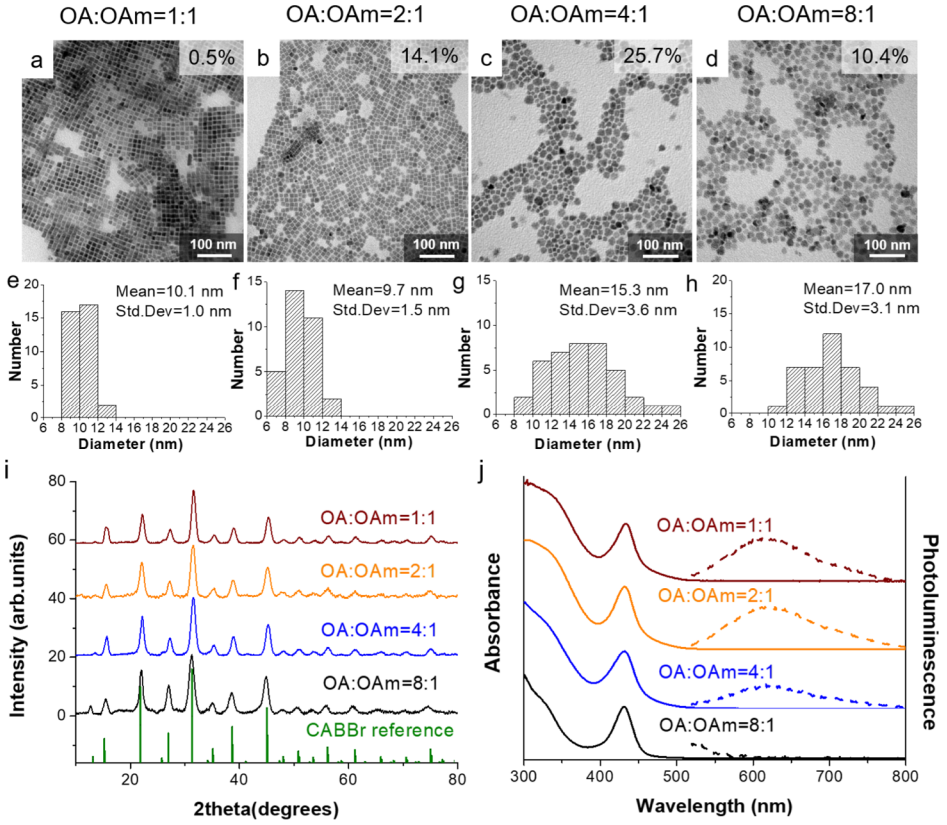

Figure 4. (a–d) TEM images, (e–h) size histograms (i) XRD, and (j) absorbance and PL emission spectra of $Cs_2AgBiBr_6$ nanocrystals synthesized with different OA to OAm mole ratios. The molar conversion (%) is shown as insets in (a–d). The mean and standard deviation of nanocrystal diameter of each histogram are provided in (e–h). XRD in (i) is performed on a nanocrystal film deposited on a glass microscope slide. The green drop lines correspond to the reference pattern for cubic $Cs_2AgBiBr_6$ (CABBr).[21] The spectra in (j) are obtained from nanocrystals dispersed in hexane. The excitation wavelength used for the PL emission spectra is λ_{exc} = 432 nm.

$$3AgBr + 3BiBr_3 + 4Cs(R'_2POO) \xrightarrow[PA,OAm,ODE]{200^\circ C,3min} 2Cs_2AgBiBr_6 + Ag(R'_2POO) + Bi(R'_2POO)_3$$
$$R' = (CH_3)_3CCH_2CH(CH_3)CH_2 \quad (2)$$

Figure 5a shows the TEM images of $Cs_2AgBiBr_6$ nanocrystals synthesized using PA and OAm. They have cuboidal shape and an aspect ratio of 1.1 ± 0.1. The short and long axes are 10.3 ± 0.9 and 11.4 ± 0.9 nm long. Figure 5b shows the XRD from the nanocrystals. They have cubic $Cs_2AgBiBr_6$ crystal structure. The comparison of absorbance and PL spectra of the nanocrystals made with OA and PA is shown in Figure 5c,d. They are similar in appearance even though the sizes are a slightly different (9.7 nm for OA and 11.0 nm for PA). Both samples show an absorption peak at 432 nm. Their broad PL peaks have the same shape and similar quantum yield. The emission at 622 nm corresponds to a band gap of 2.0 eV.

Thermal Stability of $Cs_2AgBiBr_6$ Nanocrystals. Both bulk crystals and nanocrystals of $Cs_2AgBiBr_6$ have exhibited robust thermal stability. For bulk $Cs_2AgBiBr_6$, no mass loss or phase change has been observed when heated to 450 °C.[21,23,39] The XRD pattern obtained from the $Cs_2AgBiBr_6$ nanocrystals has not changed after heating to 100 °C under dry nitrogen in the dark for 300 h.[26] To further test the thermal stability of $Cs_2AgBiBr_6$ nanocrystals, we carried out GIWAXS and GISAXS on nanocrystal films heated in situ.

Figure 6 shows the SEM, GISAXS, and GIWAXS data. Prior to heating, two Bragg rods are present in the GISAXS data in

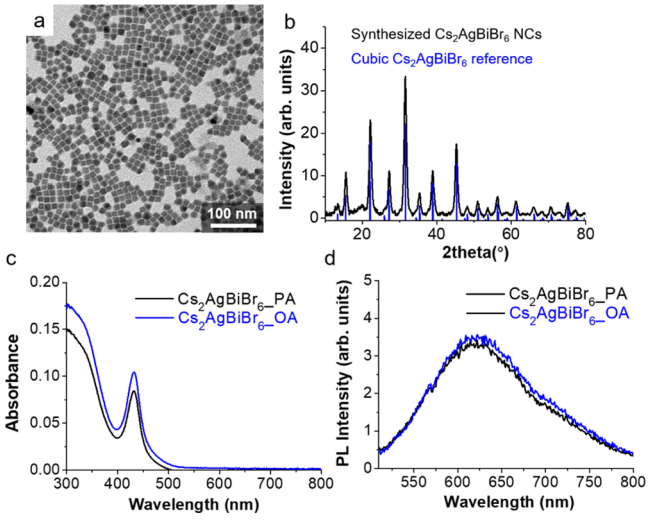

Figure 5. (a) TEM and (b) XRD of $Cs_2AgBiBr_6$ nanocrystals synthesized with PA and OAm according to eq 2. The nanocrystals have cubic shape with an average edge length of 11.0 ± 1.4 nm. The blue drop lines in (b) correspond to the cubic $Cs_2AgBiBr_6$ reference pattern.[21] Room-temperature (c) absorbance and (d) PL emission spectra (λ_{exc} = 432 nm) of $Cs_2AgBiBr_6$ nanocrystals synthesized using either PA/OAm or OA/OAm mixtures dispersed in hexane.

Figure 6b at q_x = 0.52 and q_x = 1.06 nm^{-1}, which index to {10} and {20} diffraction peaks from a cubic superlattice. These q values correspond to a center-to-center distance between

DOI: 10.1021/acs.chemmater.9b02149
Chem. Mater. 2019, 31, 7962–7969

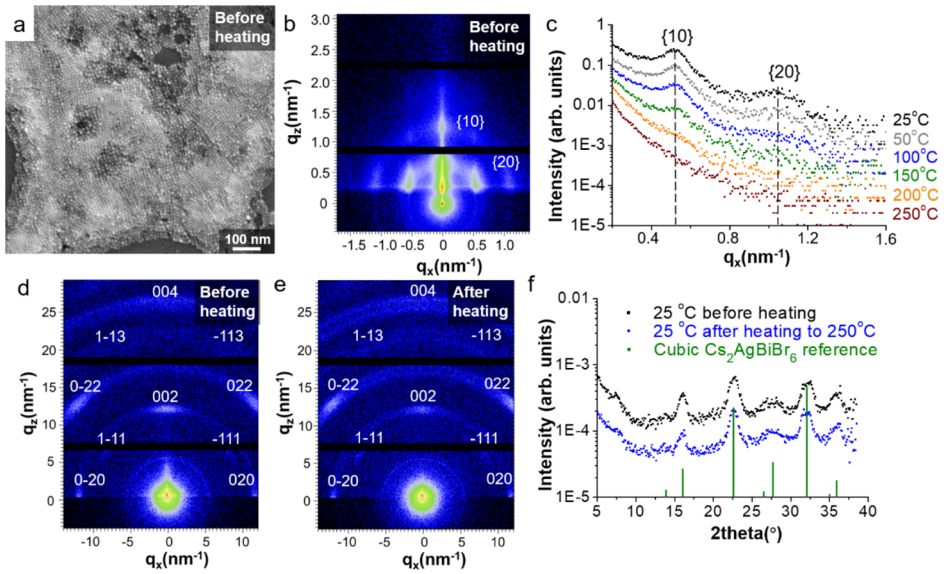

Figure 6. (a) SEM image and (b) GISAXS of $Cs_2AgBiBr_6$ nanocrystal film at 25 °C before heating. (c) Horizontal projection of GISAXS data acquired for a $Cs_2AgBiBr_6$ nanocrystal film heated in air from 25 to 250 °C. The two Bragg rods correspond to {10} and {20} peaks of a cubic superlattice. (d,e) GIWAXS of a $Cs_2AgBiBr_6$ nanocrystal film at 25 °C (d) before and (e) after heating to 250 °C. (f) Radial integrations of the GIWAXS data in (d) and (e). The green drop lines in (f) represent the cubic $Cs_2AgBiBr_6$ reference pattern.[21]

neighboring nanocrystals of 12.1 nm. The GIWAXS data (Figure 6d) index to the cubic phase of $Cs_2AgBiBr_6$. The texture indicates a preferred (001) crystallographic orientation on the substrate, which corresponds to nanocrystals lying with {002} facets. Figure 6c shows GISAXS data from the nanocrystal film heated in situ from 25 to 250 °C. The {10} and {20} peaks broaden as the temperature increases. At 200 °C, the {20} peak disappears. The {10} peak is still present and then disappears when the temperature reaches 250 °C. The nanocrystals have sintered at this temperature (see the Supporting Information, Figure S8). Even though the nanocrystals have lost their integrity, the $Cs_2AgBiBr_6$ crystal structure and orientation on the substrate does not change. The GIWAXS data before and after heating in Figure 6d,e are similar. The comparison of the data in Figure 6f reaffirms this. In comparison to other materials, the $Cs_2AgBiBr_6$ nanocrystals are similar to Au and PbSe nanocrystals, which sinter at about 200 °C, and much less than Si nanocrystals, which sinter at about 350 °C.[40−42]

Colloidal Stability of $Cs_2AgBiBr_6$ Nanocrystals. Figure 7a shows the absorbance spectra of $Cs_2AgBiBr_6$ nanocrystals dispersed in hexane that were sealed under nitrogen and exposed to room light. After 21 h, the nanocrystals have precipitated from solution. The absorbance drops to zero and the wall of the cuvette was coated with a yellow film of nanocrystals. The nanocrystals coating the cuvette could not be redispersed. The XRD patterns of the precipitated material (Figure 7b) still matched the cubic $Cs_2AgBiBr_6$ patterns, and the SEM images showed that the nanocrystals had not sintered but retained their initial size (see the Supporting Information, Figure S9). The stability of nanocrystal dispersion is also influenced by the solvent. When dispersed in toluene, the optical density of the nanocrystal dispersion dropped only slightly within 24 h. When dispersed in chloroform, the absorbance peak at 432 nm blue shifts and significantly drops in intensity (see the Supporting Information, Figure S10). The colloidal stability of these nanocrystals requires further investigation, but it is clear that light illumination leads to

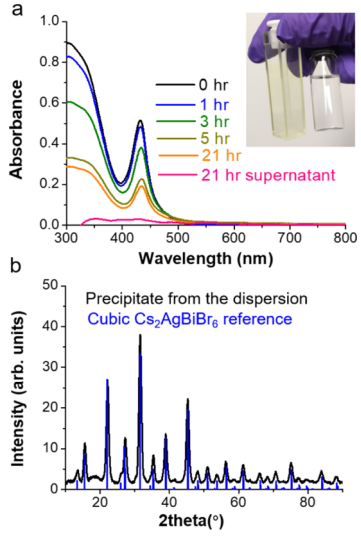

Figure 7. (a) Absorbance spectra of $Cs_2AgBiBr_6$ nanocrystals dispersed in hexane sealed under nitrogen and exposed to room light for the amount of time indicated in the caption. Inset: Photograph of the cuvette and the dispersion after 21 h of light exposure. The nanocrystals have precipitated onto the wall of the cuvette while the supernatant is clear and colorless. (b) XRD of the nanocrystals that had precipitated out of the colloidal dispersion after light exposure.

significant loss in stability in at least some solvents, even though the inorganic cores do not appear to have degraded. For $CsPbBr_3$ nanocrystals, light can induce the ligands to selectively detach from nanocrystal surface, causing the nanocrystals to self-assemble into nanowires.[43]

CONCLUSIONS

$Cs_2AgBiBr_6$ nanocrystals with cuboidal shape and cubic crystal structure were synthesized by an ionic metathesis reaction using both OAm and OA. NOESY and ^{1}H NMR showed that only OAm binds to the nanocrystal surface; however, OA is

DOI: 10.1021/acs.chemmater.9b02149
Chem. Mater. 2019, 31, 7962−7969

critical to obtaining high reaction yields. We found that OA could be replaced by PA. The $Cs_2AgBiBr_6$ nanocrystals are relatively stable, sintering at 250 °C. The cubic crystal structure of $Cs_2AgBiBr_6$ is still retained after the nanocrystals sinter, and the crystal orientation in the film is maintained. However, the colloidal stability under light in hexane is poor, and the nanocrystals precipitate after less than 24 h.

■ ASSOCIATED CONTENT

Supporting Information

The Supporting Information is available free of charge on the ACS Publications website at DOI: 10.1021/acs.chemmater.9b02149.

XRD peak fitting and size−strain analysis; EDXS elemental ratios; XRD of the black precipitate from washing; TGA data, additional HRTEM image and FFT of $Cs_2AgBiBr_6$ nanocrystals; ^1H NMR and NOESY of pure OAm and pure OA, respectively; STEM images and elemental maps of $Cs_2AgBiBr_6$ nanocrystals; SEM image of $Cs_2AgBiBr_6$ nanocrystal film after heating to 250 °C; SEM of the $Cs_2AgBiBr_6$ nanocrystals precipitated out because of room light irradiation; absorbance spectra of $Cs_2AgBiBr_6$ nanocrystals dispersed in toluene and chloroform-sealed under nitrogen and exposed to room light; and HRTEM images showing beam-induced degradation (PDF)

■ AUTHOR INFORMATION

Corresponding Author

*E-mail: korgel@che.utexas.edu.

ORCID

Yangning Zhang: 0000-0001-5511-955X
Francis Leonard Deepak: 0000-0002-3833-1775
Brian A. Korgel: 0000-0001-6242-7526

Notes

The authors declare no competing financial interest.

■ ACKNOWLEDGMENTS

Financial support of this work was provided by the Robert A. Welch Foundation (F-1464), the UT|Portugal program through the UT@INL Corner, the Industry/University Cooperative Research Center on Next Generation Photovoltaics (IIP-1540028), the Center for Dynamics and Control of Materials (CDCM) Materials Research Science and Engineering Center (MRSEC) (DMR-1720595), and NSF grant CBET-1624659. The authors thank Garrett Blake for the help in acquiring NOESY data and Steve Sorey for insightful discussions about the NOESY data.

■ REFERENCES

(1) Yettapu, G. R.; Talukdar, D.; Sarkar, S.; Swarnkar, A.; Nag, A.; Ghosh, P.; Mandal, P. Terahertz Conductivity within Colloidal $CsPbBr_3$ Perovskite Nanocrystals: Remarkably High Carrier Mobilities and Large Diffusion Lengths. *Nano Lett.* **2016**, *16*, 4838−4848.

(2) Wang, Y.; Li, X.; Zhao, X.; Xiao, L.; Zeng, H.; Sun, H. Nonlinear Absorption and Low-Threshold Multiphoton Pumped Stimulated Emission from All-Inorganic Perovskite Nanocrystals. *Nano Lett.* **2016**, *16*, 448−453.

(3) Shi, D.; Adinolfi, V.; Comin, R.; Yuan, M.; Alarousu, E.; Buin, A.; Chen, Y.; Hoogland, S.; Rothenberger, A.; Katsiev, K.; Losovyj, Y.; Zhang, X.; Dowben, P. A.; Mohammed, O. F.; Sargent, E. H.; Bakr, O. M. Low Trap-State Density and Long Carrier Diffusion in Organolead Trihalide Perovskite Single Crystals. *Science* **2015**, *347*, 519−522.

(4) Becker, M. A.; Vaxenburg, R.; Nedelcu, G.; Sercel, P. C.; Shabaev, A.; Mehl, M. J.; Michopoulos, J. G.; Lambrakos, S. G.; Bernstein, N.; Lyons, J. L.; Stöferle, T.; Mahrt, R. F.; Kovalenko, M. V.; Norris, D. J.; Rainò, G.; Efros, A. L. Bright Triplet Excitons in Caesium Lead Halide Perovskites. *Nature* **2018**, *553*, 189−193.

(5) De Weerd, C.; Gomez, L.; Capretti, A.; Lebrun, D. M.; Matsubara, E.; Lin, J.; Ashida, M.; Spoor, F. C. M.; Siebbeles, L. D. A.; Houtepen, A. J.; Suenaga, K.; Fujiwara, Y.; Gregorkiewicz, T. Efficient Carrier Multiplication in $CsPbI_3$ Perovskite Nanocrystals. *Nat. Commun.* **2018**, *9*, 4199.

(6) Utzat, H.; Sun, W.; Kaplan, A. E. K.; Krieg, F.; Ginterseder, M.; Spokoyny, B.; Klein, N. D.; Shulenberger, K. E.; Perkinson, C. F.; Kovalenko, M. V.; Bawendi, M. G. Coherent Single-Photon Emission from Colloidal Lead Halide Perovskite Quantum Dots. *Science* **2019**, *363*, 1068−1072.

(7) Nie, W.; Tsai, H.; Asadpour, R.; Blancon, J.-C.; Neukirch, A. J.; Gupta, G.; Crochet, J. J.; Chhowalla, M.; Tretiak, S.; Alam, M. A.; Wang, H.-L.; Mohite, A. D. High-Efficiency Solution-Processed Perovskite Solar Cells with Millimeter-Scale Grains. *Science* **2015**, *347*, 522−525.

(8) Swarnkar, A.; Marshall, A. R.; Sanehira, E. M.; Chernomordik, B. D.; Moore, D. T.; Christians, J. A.; Chakrabarti, T.; Luther, J. M. Quantum Dot-Induced Phase Stabilization of Alpha-$CsPbI_3$ Perovskite for High Efficiency Photovoltaics. *Science* **2016**, *354*, 92−95.

(9) Li, J.; Xu, L.; Wang, T.; Song, J.; Chen, J.; Xue, J.; Dong, Y.; Cai, B.; Shan, Q.; Han, B.; Zeng, H. 50-Fold EQE Improvement up to 6.27% of Solution-Processed All-Inorganic Perovskite $CsPbBr_3$ QLEDs via Surface Ligand Density Control. *Adv. Mater.* **2017**, *29*, 1603885.

(10) Eaton, S. W.; Lai, M.; Gibson, N. A.; Wong, A. B.; Dou, L.; Ma, J.; Wang, L.-W.; Leone, S. R.; Yang, P. Lasing in Robust Cesium Lead Halide Perovskite Nanowires. *Proc. Natl. Acad. Sci.* **2016**, *113*, 1993−1998.

(11) Ahmadi, M.; Wu, T.; Hu, B. A Review on Organic-Inorganic Halide Perovskite Photodetectors: Device Engineering and Fundamental Physics. *Adv. Mater.* **2017**, *29*, 1605242.

(12) Protesescu, L.; Yakunin, S.; Bodnarchuk, M. I.; Krieg, F.; Caputo, R.; Hendon, C. H.; Yang, R. X.; Walsh, A.; Kovalenko, M. V. Nanocrystals of Cesium Lead Halide Perovskites ($CsPbX_3$, X = Cl, Br, and I): Novel Optoelectronic Materials Showing Bright Emission with Wide Color Gamut. *Nano Lett.* **2015**, *15*, 3692−3696.

(13) Shamsi, J.; Urban, A. S.; Imran, M.; De Trizio, L.; Manna, L. Metal Halide Perovskite Nanocrystals: Synthesis, Post-Synthesis Modifications, and Their Optical Properties. *Chem. Rev.* **2019**, *119*, 3296−3348.

(14) Huang, H.; Bodnarchuk, M. I.; Kershaw, S. V.; Kovalenko, M. V.; Rogach, A. L. Lead Halide Perovskite Nanocrystals in the Research Spotlight: Stability and Defect Tolerance. *ACS Energy Lett.* **2017**, *2*, 2071−2083.

(15) Siegler, T. D.; Houck, D. W.; Cho, S. H.; Milliron, D. J.; Korgel, B. A. Bismuth Enhances the Stability of $CH_3NH_3PbI_3$ (MAPI) Perovskite under High Humidity. *J. Phys. Chem. C* **2019**, *123*, 963−970.

(16) Noel, N. K.; Stranks, S. D.; Abate, A.; Wehrenfennig, C.; Guarnera, S.; Haghighirad, A. A.; Sadhanala, A.; Eperon, G. E.; Johnston, M. B.; Petrozza, A. M.; Herz, L. M.; Snaith, H. J. Lead-Free Organic-Inorganic Tin Halide Perovskites for Photovoltaic Applications. *Energy Environ. Sci.* **2014**, *7*, 3061−3068.

(17) Kopacic, I.; Friesenbichler, B.; Hoefler, S. F.; Kunert, B.; Plank, H.; Rath, T.; Trimmel, G. Enhanced Performance of Germanium Halide Perovskite Solar Cells through Compositional Engineering. *ACS Appl. Energy Mater.* **2018**, *1*, 343−347.

(18) Giustino, F.; Snaith, H. J. Toward Lead-Free Perovskite Solar Cells. *ACS Energy Lett.* **2016**, *1*, 1233−1240.

(19) Zhao, X.-G.; Yang, J.-H.; Fu, Y.; Yang, D.; Xu, Q.; Yu, L.; Wei, S.-H.; Zhang, L. Design of Lead-Free Inorganic Halide Perovskites for

DOI: 10.1021/acs.chemmater.9b02149
Chem. Mater. 2019, 31, 7962−7969

Solar Cells via Cation-Transmutation. *J. Am. Chem. Soc.* **2017**, *139*, 2630−2638.
(20) Mcclure, E. T.; Ball, M. R.; Windl, W.; Woodward, P. M. Cs_2AgBiX_6 (X = Br,Cl): New Visible Light Absorbing, Lead-Free Halide Perovskite Semiconductors. *Chem. Mater.* **2016**, *28*, 1348−1354.
(21) Slavney, A. H.; Hu, T.; Lindenberg, A. M.; Karunadasa, H. I. A Bismuth-Halide Double Perovskite with Long Carrier Recombination Lifetime for Photovoltaic Applications. *J. Am. Chem. Soc.* **2016**, *138*, 2138−2141.
(22) Igbari, F.; Wang, R.; Wang, Z.-K.; Ma, X.-J.; Wang, Q.; Wang, K.-L.; Zhang, Y.; Liao, L.-S.; Yang, Y. Composition Stoichiometry of $Cs_2AgBiBr_6$ Films for Highly Efficient Lead-Free Perovskite Solar Cells. *Nano Lett.* **2019**, *19*, 2066−2073.
(23) Gao, W.; Ran, C.; Xi, J.; Jiao, B.; Zhang, W.; Wu, M.; Hou, X.; Wu, Z. High-Quality $Cs_2AgBiBr_6$ Double Perovskite Film for Lead-Free Inverted Planar Heterojunction Solar Cells with 2.2% Efficiency. *ChemPhysChem* **2018**, *19*, 1696−1700.
(24) Creutz, S. E.; Crites, E. N.; De Siena, M. C.; Gamelin, D. R. Colloidal Nanocrystals of Lead-Free Double-Perovskite (Elpasolite) Semiconductors: Synthesis and Anion Exchange To Access New Materials. *Nano Lett.* **2018**, *18*, 1118−1123.
(25) Bekenstein, Y.; Dahl, J. C.; Huang, J.; Osowiecki, W. T.; Swabeck, J. K.; Chan, E. M.; Yang, P.; Alivisatos, A. P. The Making and Breaking of Lead-Free Double Perovskite Nanocrystals of Cesium Silver-Bismuth Halide Compositions. *Nano Lett.* **2018**, *18*, 3502−3508.
(26) Zhou, L.; Xu, Y.-F.; Chen, B.-X.; Kuang, D.-B.; Su, C.-Y. Synthesis and Photocatalytic Application of Stable Lead-Free $Cs_2AgBiBr_6$ Perovskite Nanocrystals. *Small* **2018**, *14*, 1703762.
(27) Locardi, F.; Cirignano, M.; Baranov, D.; Dang, Z.; Prato, M.; Drago, F.; Ferretti, M.; Pinchetti, V.; Fanciulli, M.; Brovelli, S.; De Trizio, L.; Manna, L. Colloidal Synthesis of Double Perovskite $Cs_2AgInCl_6$ and Mn-Doped $Cs_2AgInCl_6$ Nanocrystals. *J. Am. Chem. Soc.* **2018**, *140*, 12989−12995.
(28) Dahl, J. C.; Osowiecki, W. T.; Cai, Y.; Swabeck, J. K.; Bekenstein, Y.; Asta, M.; Chan, E. M.; Alivisatos, A. P. Probing the Stability and Band Gaps of $Cs_2AgInCl_6$ and $Cs_2AgSbCl_6$ Lead-Free Double Perovskite Nanocrystals. *Chem. Mater.* **2019**, *31*, 3134−3143.
(29) Smilgies, D.-M.; Blasini, D. R. Indexation Scheme for Oriented Molecular Thin Films Studied with Grazing-Incidence Reciprocal-Space Mapping. *J. Appl. Crystallogr.* **2007**, *40*, 716−718.
(30) Guillaussier, A.; Yu, Y.; Voggu, V. R.; Aigner, W.; Cabezas, C. S.; Houck, D. W.; Shah, T.; Smilgies, D.-M.; Pereira, R. N.; Stutzmann, M.; Korgel, B. A. Silicon Nanocrystal Superlattice Nucleation and Growth. *Langmuir* **2017**, *33*, 13068−13076.
(31) van der Burgt, J. S.; Geuchies, J. J.; van der Meer, B.; Vanrompay, H.; Zanaga, D.; Zhang, Y.; Albrecht, W.; Petukhov, A. V.; Filion, L.; Bals, S.; Swart, I. Cuboidal Supraparticles Self-Assembled from Cubic $CsPbBr_3$ Perovskite Nanocrystals. *J. Phys. Chem. C* **2018**, *122*, 15706−15712.
(32) Levitt, M. H. *Spin Dynamics-Basics of Nuclear Magnetic Resonance*; Wiley: Chichester, U.K., 2001.
(33) De Roo, J.; Ibáñez, M.; Geiregat, P.; Nedelcu, G.; Walravens, W.; Maes, J.; Martins, J. C.; Van Driessche, I.; Kovalenko, M. V.; Hens, Z. Highly Dynamic Ligand Binding and Light Absorption Coefficient of Cesium Lead Bromide Perovskite Nanocrystals. *ACS Nano* **2016**, *10*, 2071−2081.
(34) Ravi, V. K.; Santra, P. K.; Joshi, N.; Chugh, J.; Singh, S. K.; Rensmo, H.; Ghosh, P.; Nag, A. Origin of the Substitution Mechanism for the Binding of Organic Ligands on the Surface of $CsPbBr_3$ Perovskite Nanocubes. *J. Phys. Chem. Lett.* **2017**, *8*, 4988−4994.
(35) Houck, D. W.; Korgel, B. A. Facile Exchange of Tightly Bonded L-Type Oleylamine and Diphenylphosphine Ligands on Copper Indium Diselenide Nanocrystals Mediated by Molecular Iodine. *Chem. Mater.* **2018**, *30*, 8359−8367.
(36) Hens, Z.; Martins, J. C. A Solution NMR Toolbox for Characterizing the Surface Chemistry of Colloidal Nanocrystals. *Chem. Mater.* **2013**, *25*, 1211−1221.
(37) Almeida, G.; Goldoni, L.; Akkerman, Q.; Dang, Z.; Khan, A. H.; Marras, S.; Moreels, I.; Manna, L. Role of Acid−Base Equilibria in the Size, Shape, and Phase Control of Cesium Lead Bromide Nanocrystals. *ACS Nano* **2018**, *12*, 1704−1711.
(38) Wang, C.; Chesman, A. S. R.; Jasieniak, J. J. Stabilizing the Cubic Perovskite Phase of $CsPbI_3$ Nanocrystals by Using an Alkyl Phosphinic Acid. *Chem. Commun.* **2017**, *53*, 232−235.
(39) Schade, L.; Wright, A. D.; Johnson, R. D.; Dollmann, M.; Wenger, B.; Nayak, P. K.; Prabhakaran, D.; Herz, L. M.; Nicholas, R.; Snaith, H. J.; Radaelli, P. G. Structural and Optical Properties of $Cs_2AgBiBr_6$ Double Perovskite. *ACS Energy Lett.* **2019**, *4*, 299−305.
(40) Goodfellow, B. W.; Rasch, M. R.; Hessel, C. M.; Patel, R. N.; Smilgies, D.-M.; Korgel, B. A. Ordered Structure Rearrangements in Heated Gold Nanocrystal Superlattices. *Nano Lett.* **2013**, *13*, 5710−5714.
(41) Goodfellow, B. W.; Patel, R. N.; Panthani, M. G.; Smilgies, D.-M.; Korgel, B. A. Melting and Sintering of a Body-Centered Cubic Superlattice of PbSe Nanocrystals Followed by Small Angle X-ray Scattering. *J. Phys. Chem. C* **2011**, *115*, 6397−6404.
(42) Yu, Y.; Bosoy, C. A.; Smilgies, D.-M.; Korgel, B. A. Self-Assembly and Thermal Stability of Binary Superlattices of Gold and Silicon Nanocrystals. *J. Phys. Chem. Lett.* **2013**, *4*, 3677−3682.
(43) Liu, J.; Song, K.; Shin, Y.; Liu, X.; Chen, J.; Yao, K. X.; Pan, J.; Yang, C.; Yin, J.; Xu, L.-J.; Yang, H.; El-Zohry, A. M.; Xin, B.; Mitra, S.; Hedhili, M. N.; Roqan, I. S.; Mohammed, O. F.; Han, Y.; Bakr, O. M. Light-Induced Self-Assembly of Cubic $CsPbBr_3$ Perovskite Nanocrystals into Nanowires. *Chem. Mater.* **2019**, *31*, 6642−6649.

DOI: 10.1021/acs.chemmater.9b02149
Chem. Mater. 2019, 31, 7962−7969